

Rapid Wireless Capacitor Charging using a Multi-Tapped Inductively-Coupled Secondary Coil

Patrick P. Mercier, *Member, IEEE* and Anantha P. Chandrakasan, *Fellow, IEEE*

Abstract—This paper presents an inductive coupling system designed to wirelessly charge ultra-capacitors used as energy storage elements. Although ultra-capacitors offer the native ability to rapidly charge, it is shown that standard inductive coupling circuits only deliver maximal power for a specific load impedance which depends on coil geometries and separation distances. Since a charging ultra-capacitor can be modeled as an increasing instantaneous impedance, maximum power is thus delivered to the ultra-capacitor at only a single point in the charging interval, resulting in a longer than optimal charging time. Analysis of inductive coupling theory reveals that the optimal load impedance can be modified by adjusting the secondary coil inductance and resonant tuning capacitance. A three-tap secondary coil is proposed to dynamically modify the optimal load impedance throughout the capacitor charging interval. Measurement results show that the proposed architecture can expand its operational range by up to 2.5X and charge a 2.5F ultra-capacitor to 5V upwards of 3.7X faster than a conventional architecture.

Index Terms—wireless power transfer, inductive coupling, multi-tap inductor, capacitor charging, ultra-capacitor

I. INTRODUCTION

NEAR-field inductive wireless power transfer is an increasingly popular method to chronically deliver power to electronic devices that are otherwise difficult to interface with using direct wired connections. Applications are vast and include, among many others, implanted medical devices [1], [2], radio frequency identification (RFID) products [3], and non-contact semiconductor testers [4]. On the other hand, there are several application spaces where power is not delivered chronically, but is instead delivered over a finite amount of time, typically to periodically charge an energy storage element – for example wireless battery charging in consumer electronics, semi-active RFID, and electric vehicles [5]–[8].

Periodic charging of an energy storage element can in fact be a favorable alternative use-case for applications that traditionally employ chronic wireless power delivery. For example, biomedical implants could benefit greatly from both aesthetic and usability perspectives if the entire system can be fully implantable, eliminating the requirement of a semi-permanent external energy source. In this manner, a patient could retain the implant’s functionality, even when performing tasks that are not conducive to wearing an external device (e.g., taking

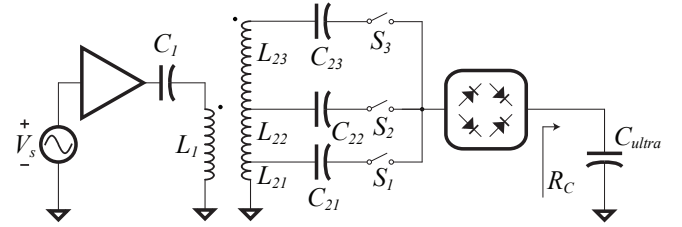


Fig. 1. Architecture of the multi-tapped secondary inductive coupling system.

a shower or going swimming). However, the volume available to store energy within implants, portable consumer electronics, or electric vehicles is limited, and as a result, recharging must occur frequently. Unfortunately, batteries are slow to charge and can only do so a finite number of times, thereby requiring eventual, and potentially very expensive, replacement.

On the other hand, ultra-capacitors can support at least 1,000,000 re-charge cycles [9], potentially never requiring replacement over the useful lifetime of a device. The energy storage density of commercially available ultra-capacitors is, however, lower than batteries by approximately 30X [10], [11], although future research directions expect to decrease this gap significantly [12]. Additional power management is also required for devices utilizing ultra-capacitors as energy sources, in order to regulate the output voltage [13], [14]. The salient saving feature of ultra-capacitors as energy storage elements is their ability to rapidly charge. Unlike batteries, which can take hours to charge, ultra-capacitors can charge nearly instantly, limited only by power density or heat dissipation limits. From a user’s perspective, convenient rapid charging can potentially offset the requirement of charging more frequently.

To this end, periodically charging an ultra-capacitor through an inductively coupled link presents a different problem formulation. Unlike chronic wireless power delivery systems which endeavor to maximize power transfer efficiency, the goal of this work is to instead *minimize charging time*. From a design perspective, this is equivalent to maximizing the amount of power delivered to the ultra-capacitor over transient conditions, given source and system constraints. Prior work in related areas focused either on resistive loads [15]–[17], utilized similar techniques to those used for resistive loads [18], or used alternative methods of ultra-capacitor charging that may not be suitable for all applications (e.g., solar [19]).

As will be shown in Section II, given a set of inductively coupled coil size and spacing geometries, a maximum power transfer condition occurs for a specific load impedance. This work presents an inductive coupling architecture that employs a multi-tapped secondary, as shown in Fig. 1, in order to

Patrick P. Mercier is with the Department of Electrical and Computer Engineering, University of California at San Diego, La Jolla, CA 92093-0407 USA (e-mail: pmercier@ucsd.edu).

Anantha Chandrakasan is with the Department of Electrical Engineering and Computer Science, Massachusetts Institute of Technology (MIT), Cambridge, MA 02139 USA.

Copyright (c) 2013 IEEE. Personal use of this material is permitted. However, permission to use this material for any other purposes must be obtained from the IEEE by sending an email to pubs-permissions@ieee.org

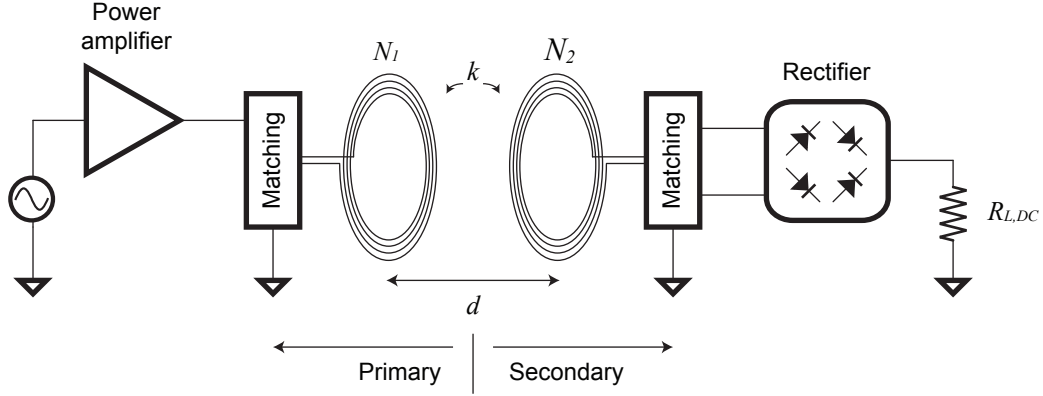


Fig. 2. Typical block diagram of an inductive coupling setup driving a resistive load.

dynamically modify the coil geometries, which in turn modify the optimal load impedance. This presents an opportunity to dynamically adjust the optimal load impedance to match the actual instantaneous load impedance of the charging capacitor. Measurement results of a discrete prototype are shown in Section IV, and the paper concludes with a summary in Section V.

II. INDUCTIVE COUPLING THEORY: MAXIMUM POWER TRANSFER

A. Overview and Definitions

An illustration of a typical inductive coupling system is shown in Fig. 2. The circuit operates as follows: a power amplifier, with an RF voltage-source input, sends power through a primary-side coil with N_1 turns. Matching is used to tune-out the inherent loop inductance in order to decrease loading effects on the power amplifier. So long as the operational wavelength is much less than the physical dimension of the coils and their separation, energy will be contained solely in near-field magnetics. Thus, the secondary-side coil, composed on N_2 turns and spaced a distance d from the primary-side coil, receives energy from the transmitter's produced time-varying magnetic field. The RF output of the secondary-side matching network then passes through a rectifier, converting the AC energy into DC energy used to power the load, in this case modeled by resistor $R_{L,DC}$.

Since the coils are well-modeled by lumped inductors under near-field approximations, the matching networks typically consist of either series or parallel capacitors. Sizing these capacitors to resonate with their respective inductors at the frequency of power transfer has been shown to maximize efficiency and minimize loading of the power amplifier [15]. On the primary, series-tuning is typically employed for voltage-source drivers (i.e., most class-A through class-F power amplifiers). The choice of secondary-side tuning depends greatly on the application. It is well known that using a parallel secondary tuning capacitance induces a voltage multiplication factor, making rectifier diodes easier to turn-on. This makes a series-parallel link configuration ideal for low-power (i.e., high R_L) applications, where it is difficult to generate sufficient voltage

to activate non-linear rectifiers. At high powers (i.e., low R_L), the voltage multiplication factor may present voltages that go far beyond CMOS or diode compatibility, limiting its utility. Instead, a series-series link is preferred for high power applications, where increased power is delivered through Q-multiplied current rather than voltage.

A more detailed circuit diagram of a typical inductive coupled system for high power applications is shown in Fig. 3. Inductors L_1 and L_2 model the primary and secondary loop reactances, respectively. The quality factor of each coil is given by $Q_{1,2} = \omega L_{1,2}/R_{1,2}$, where ω is the operating frequency and $R_{1,2}$ represents the parasitic series loss resistance. Voltage sources sMi_2 and sMi_1 model the mutual coupling effects between the coils, where M is the mutual coupling factor, while capacitors C_1 and C_2 provide resonant matching with the inductors. The coil coupling coefficient, k , is defined by the following equation:

$$k \equiv \frac{M}{\sqrt{L_1 L_2}}. \quad (1)$$

It can be shown that k is dependent only on coil separation distance d and individual coil geometries [15]. Importantly, it should be noted that k varies between 0 (no coupling) and 1 (perfect coupling), and decreases with d .

The primary side is driven by a voltage source, V_s , that has a series resistance, R_s . The secondary side is loaded by a resistor, R_L . Note that the actual load circuits are always found at the output of the rectifier. However, it can be easily shown that, with respect to the schematic in Fig. 2, $R_L \approx R_{L,DC}/2$ [15]. Finally, an important definition that will be useful for analysis is the turns ratio of an ideal transformer, assuming perfect coupling:

$$n \equiv \sqrt{\frac{L_2}{L_1}}. \quad (2)$$

B. Reflected Load Analysis

Inductive coupling theory has been well-studied in the past, and many excellent references describe analytical expressions that can accurately predict the maximum achievable efficiency

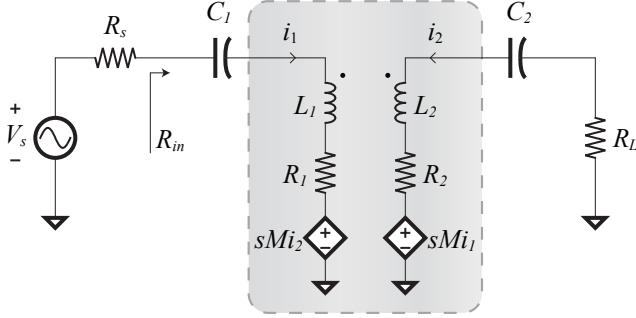


Fig. 3. Inductive coupling circuit model using series-series capacitive tuning.

of a given link [15]–[17]. However, the new problem formulation of maximizing power transfer requires new analysis to determine optimal design conditions. Building on existing work, this section derives new analytical results for predicting maximum power transfer conditions. Although a series-tuned secondary is considered here, the results can be easily extended to a parallel-tuned secondary by employing a parallel-to-series impedance transformation [20]. It is important to note, however, that resonance can be achieved when converting a parallel load impedance, $R_{L,p}$, to a series equivalent, R_L , only if $1/R_{L,p}^2 C_2^2 > 1/L_2 C_2$. For low values of $R_{L,p}$ (i.e., higher power applications), this will not always be the case; this is a further reason to use a series-tuned secondary. Otherwise, a primary circuit that senses this condition and shifts its driving frequency would be necessary to compensate for this effect [21].

In order to determine what conditions permit transfer of maximum power to the load, it is necessary to obtain workable expressions for simplified, though equivalent circuits. It is well known that the inductive coupling circuit in Fig. 3 can be modeled with an ideal transformer with turns ratio n/k , leakage inductance $L_1(1 - k^2)$, and magnetizing inductance L_2 , as shown in Fig. 4(a). It is also well-known that circuit elements can be reflected across the terminals of an ideal transformer via a multiplicative factor of $(k/n)^2$. This is the basis for reflected load analysis. Similar analysis of the circuit in Fig. 2 can be performed using coupled-mode theory as generally preferred by physicists [22], though such analysis has been shown to be equivalent to reflected load analysis under near-field approximations with relatively low coupling coefficients and high quality factors [23]. Since reflected load analysis is valid over a larger range of assumptions, it is used as the main vehicle of analysis for this paper.

To gain design insight through simplified yet equivalent circuits, the total non-inductive secondary impedances in Fig. 4(a) are grouped together such that they exist in parallel to L_2 for reflection to the primary side. The total secondary impedance is given by $Z_{2T} = R_2 + R_L + 1/j\omega C_2$ and is shown reflected to the primary side in Fig. 4(b).

Due to the parallel combination of an inductance and complex impedance, Fig. 4(b) is still too cumbersome for practical analysis. Mapping the values in Fig. 4(b) to Fig. 4(c) is the next step in enabling useful analysis. This can be done

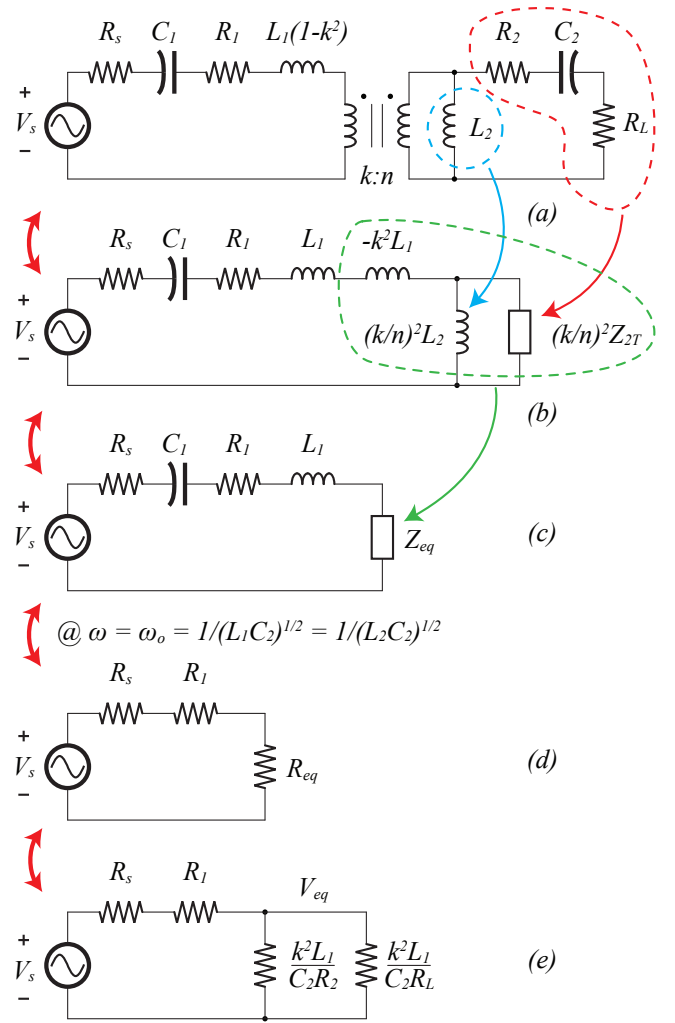


Fig. 4. Equivalent circuit models using reflected load analysis to determine analytical expressions for maximum power transfer.

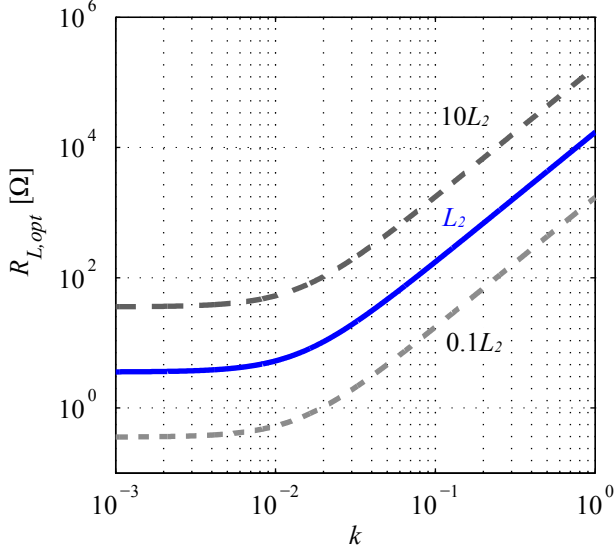
as follows¹:

$$\begin{aligned}
 Z_{eq} &= -j\omega k^2 L_1 + \frac{1}{\frac{1}{j\omega(k/n)^2 L_2} + \frac{1}{(k/n)^2 Z_{2T}}} \\
 &= -j\omega k^2 L_1 + \frac{1}{\frac{1}{j\omega k^2 L_1} + \frac{1}{(k/n)^2 Z_{2T}}} \\
 &= \frac{\omega^3 k^2 L_1 L_2 C_2 [\omega C_2 (R_L + R_2) + j(1 - \omega^2 L_2 C_2)]}{\omega^2 C_2^2 (R_L + R_2)^2 + (1 - \omega^2 L_2 C_2)^2}.
 \end{aligned} \tag{3}$$

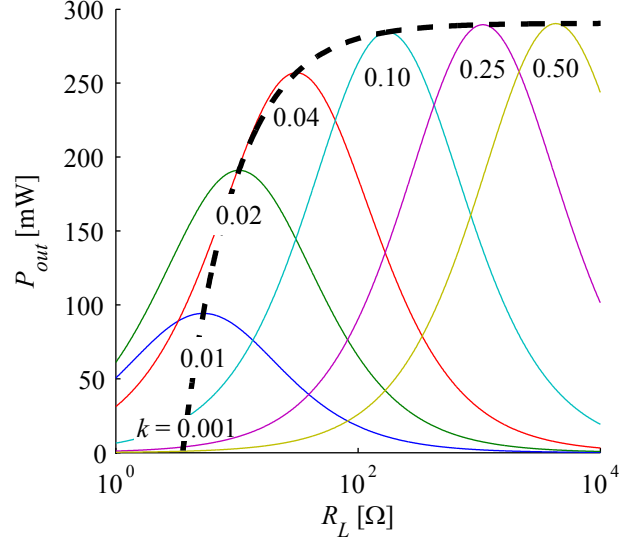
However, Equation 3 is not very insightful for analysis. Fortunately, the expression simplifies considerably at resonance (i.e., $\omega = \omega_o = 1/\sqrt{L_2 C_2}$):

$$Z_{eq}|_{\omega_o} = \frac{k^2 L_1}{C_2 (R_L + R_2)} = R_{eq}. \tag{4}$$

¹This result was also shown in [17].



(a) Load impedances that maximize power transfer plotted across all practically useful coupling coefficients for various values of L_2 .



(b) Amount of extracted output power plotted across a range of load resistances for various values of k (whose values are annotated in plain text on the figure). The solid dashed line represents the maximum extractable power for a given k .

Fig. 5. Load impedances that maximize power transfer. In this example, $V_s = 3.3 V_{p-p}$, $f = 6.78$ MHz, $L_1 = 3.3 \mu H$, $L_{2,nom} = 6.7 \mu H$, $Q_1 = 60$, and $Q_2 = 80$.

What is critical to note here is that this is a purely real impedance. The equivalent circuit under this resonant condition is shown in Fig. 4(d), assuming that L_1 and C_1 are also designed to resonate at the same frequency as the secondary (i.e., $\omega = \omega_o = 1/\sqrt{L_1 C_1} = 1/\sqrt{L_2 C_2}$), thereby shorting themselves out at the resonant frequency. The expression for R_{eq} can then be split into two different components as follows:

$$\begin{aligned} R_{eq} &= \frac{k^2 L_1}{C_2(R_L + R_2)} \\ &= \frac{k^2 L_1}{C_2} \left(\frac{R_L R_2}{R_L + R_2} \right) \frac{1}{R_L R_2} \\ &= \left(\frac{k^2 L_1}{C_2 R_2} \right) \parallel \left(\frac{k^2 L_1}{C_2 R_L} \right). \end{aligned} \quad (5)$$

A circuit with these two separated components is shown in Fig. 4(e). Given that there is an isolated component proportional to the load resistor, the power consumption seen at the load can be found using the following set of equations:

$$\begin{aligned} P_{out} &= V_{eq,rms}^2 \left(\frac{C_2 R_L}{k^2 L_1} \right) \\ V_{eq,rms} &= V_{s,rms} \left(\frac{R_{eq}}{R_s + R_1 + R_{eq}} \right) \\ &= V_{s,rms} \left(\frac{k^2 L_1}{C_2(R_s + R_1)(R_L + R_2) + k^2 L_1} \right) \\ P_{out} &= V_{s,rms}^2 \left(\frac{k^2 L_1 C_2 R_L}{(k^2 L_1 + C_2(R_s + R_1)(R_L + R_2))^2} \right). \end{aligned} \quad (6)$$

Solving the following equation can lead to the load impedance that maximizes power transfer, given all other inductive cou-

pling conditions:

$$\frac{\partial P_{out}}{\partial R_L} = 0. \quad (7)$$

The solution to this equation is shown here:

$$R_{L,opt} = R_2 + \frac{k^2 L_1}{C_2(R_s + R_1)}. \quad (8)$$

Lumping R_s together with R_1 and substituting R 's for Q 's and L 's further simplifies the equation:

$$\begin{aligned} R_{L,opt} &= \frac{\omega L_2}{Q_2} + \frac{k^2 Q_1}{\omega C_2} \\ &= \frac{1}{Q_2} \sqrt{\frac{L_2}{C_2}} + k^2 Q_1 \sqrt{\frac{L_2}{C_2}} \\ &= \sqrt{\frac{L_2}{C_2}} \left(\frac{1 + k^2 Q_1 Q_2}{Q_2} \right). \end{aligned} \quad (9)$$

Remarkably, this is a very similar to expression of load impedance that maximizes power transfer efficiency (see the appendix for further details).

Equation 9 shows that the ideal load impedance (i.e., the value of R_L that maximizes power transfer to itself) changes with the coupling coefficient, k . It is also dependent on the ratio of secondary reactance values and the coil quality factors. Thus, the optimal impedance depends on the separation between coils, as well as their geometries. Figure 5a plots the optimal load impedances across all practical values of k for the particular inductive parameters indicated in the figure caption. In this example, R_L varies from a minimum of 3.6 Ω at $k \approx 0$, to a maximum of 17 k Ω at $k = 1$. Interestingly, the optimal R_L at low coupling coefficients is exactly equal to the parasitic resistance of the secondary coil, R_2 , as can

be inferred by Equation 8. This matches intuition well, since the state of the secondary circuit has almost no bearing on the primary circuit under low coupling conditions (i.e., its reflected impedance to the primary is negligible), and thus a maximum power matching circuit on the secondary is the configuration that extracts the most power. At higher levels of coupling, reflected impedances are no longer negligible. Thus, matching R_L to R_2 would significantly load the primary circuit, thereby falling out of a maximum power transfer condition.

Figure 5b shows the extractable output power from the same inductive coupling setup as described in Fig. 5a, but this time plotted for varying output loads and coupling coefficients. Also shown is the maximum theoretically attainable output power and the associated load resistances for k varying from 0.001 to 0.5. At low coupling coefficients, the optimal R_L is small, as is the maximum extractable power. As k increases, the optimal R_L and associated extractable power increases. Although $R_{L,opt}$ continues to increase with k , $P_{out,max}$ sees diminishing returns due to the fixed source impedance, eventually plateauing beyond coupling coefficients greater than 0.2. In other words, at high values of k , the reflection coefficient becomes large, requiring a large R_L (due to the inverse relationship) to create an impedance that matches $R_1 + R_s$. At this point, the reflected $k^2 L_1 / (C_2 R_2)$ becomes very large relative to $k^2 L_1 / (C_2 R_L)$, making its effects negligible. Thus, the maximum power transfer theory can be simply applied here: $k^2 L_1 / (C_2 R_L) = R_1 + R_s$, resulting in a maximum of 50% power transfer efficiency.

C. Charging Capacitor Model

AC to DC converters employ the use of non-linear elements such as diodes to perform rectification. This makes rectifier modeling challenging, as large-signal analysis is typically required. Although charging a capacitor is by definition a transient event, it is possible to generate a model using a quasi-steady-state approximation. Specifically, a charging capacitor can be modeled over a sufficiently short period of time (given the size of the capacitor and input current) as a DC voltage source. At steady-state, a rectifier feeding a DC voltage source can be modeled as a resistor whose resistance depends on the input voltage, output voltage, and diode characteristics [24]. Thus, a charging capacitor can be modeled as a resistor, R_C , whose resistance instantaneously changes as the voltage on the capacitor increases.

III. MULTI-TAPPED SECONDARY DESIGN

A. Theory

A capacitor whose instantaneous resistance, R_C , changes with its increasing output voltage is an issue when using an inductively-coupled charging system: since there is an optimum impedance that maximizes power transfer to the load, there is at most only a single point in time during the capacitor charging interval at which it is charging at the maximum possible rate (i.e., when $R_C = R_{L,opt}$). To overcome this issue and provide maximum power for larger portions of the charging time, a proposed solution could alter the effective load impedance using an additional matching network (e.g.,

[25]) or an output DC/DC converter. However, given finite passive quality factors, it is difficult to achieve large impedance transformation ratios at high efficiencies.

Instead, Equation 9 shows that the optimal impedance depends on the ratio of secondary reactances: $\sqrt{L_2/C_2}$. Under resonant conditions, L_2 and C_2 are naturally related by the following relation: $\omega_o = 1/\sqrt{L_2 C_2}$. Thus, the optimal impedance for maximum power transfer shown in Equation 9 can be re-written in terms of either C_2 or L_2 , the latter of which is shown here:

$$R_{L,opt} = \omega_o L_2 \left(\frac{1 + k^2 Q_1 Q_2}{Q_2} \right). \quad (10)$$

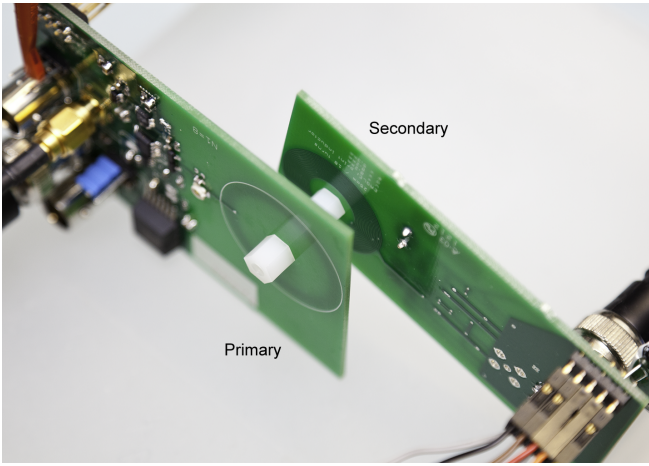
Changing the value of L_2 (and, correspondingly, C_2) can therefore change $R_{L,opt}$ for a given k , as shown in Fig. 5a. Such a circuit can, at any point in time and for any k , change $R_{L,opt}$ to equal the charging capacitor's instantaneous resistance (R_C) at that precise instance in time. This secondary reactance modulation technique can be performed dynamically to provide robustness to instantaneously changing load impedances, or it can be performed semi-statically to provide robustness against variations in coil separation distances, all while decreasing charging time. Although tunable inductors are often difficult to implement, others have described and validated such circuits for RFIC applications using interesting bridge topologies [26] or multi-tap structures [27].

B. Implementation

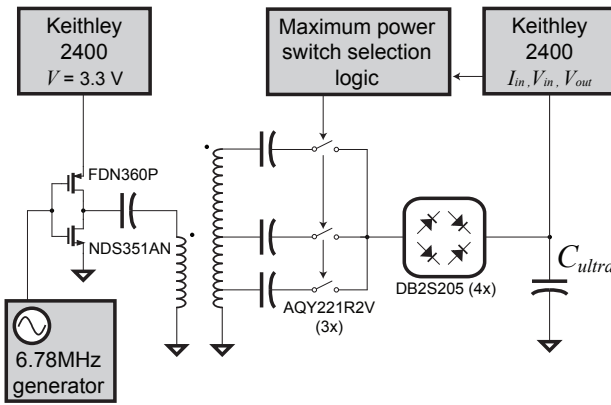
1) *Architecture*: The architecture of the proposed multi-tap-secondary inductive coupling system for rapid wireless capacitor charging is shown in Fig. 1, and a photograph and schematic of the testing setup is shown in Fig. 6. The secondary coil is designed as a single large coil with inductance L_{23} . Two smaller inductances, L_{22} and L_{21} , are created by tapping into fewer turns of the coil. Each tap is allocated a single series capacitor used to resonate with the effective inductance seen at the output of the tap. The output of the series capacitors are connected to series switches, used to select a single tap configuration at a time.

The number of taps and turns selected for each additional tap can be selected at design time by considering the range of expected values of R_L and k , and ensuring that adequate power transfer is achieved over this range. For example, the design recipe described in [17], together with the equations presented in this paper for maximum power transfer (rather than efficiency), can be used as a starting point to analytically determine the desired inductances, given R_L and k bounds. Electromagnetic simulation or experimentation can then be used to refine tap selections.

To have minimal effect on the inductor quality factors, the series tap-selection switches should be designed with as low on-resistance as possible. However, low-impedance switches typically have large associated parasitic capacitances. Additionally complicating the matter is the need for high voltage-blocking capabilities due to the (loaded) Q voltage multiplication on unused taps. The best trade-off here is to select a switch whose impedance is minimal, while offering sufficient voltage blocking capability and parasitic capacitance



(a)



(b)

Fig. 6. Photograph (a) and schematic (b) of the testing setup for the rapid wireless capacitor charger.

that does not overwhelm or appreciable change the resonant frequency set by the series capacitors.

As discussed in more detail in the following subsection, the discrete prototype design employs the use of a secondary inductor that is 25 mm in diameter. At this size, a total of 20 turns achieves an approximate inductance of less than 10 μH . At the operational frequency of 6.78 MHz used throughout this paper, such an inductor size results in a minimum series tuning capacitance of approximately 50 pF. For a proof-of-concept prototype, a Panasonic AQY221R2V solid-state optoelectronic relay was chosen as the switching element, as its on-resistance is 0.75 Ω , its parasitic capacitance is 12.5 pF, and it can safely block 40 V. When turned on, the relay requires approximately 5 mW to operate.²

Many inductively-coupled applications employ the use of class-E power amplifiers on the primary circuit for high efficiency [28]. However, a class-E amplifier requires very precise knowledge of the load impedance in order to operate properly (and therefore at high efficiency) [20]. As previously discussed, inductive coupling systems operating with

²Future work involving switch integration and/or miniaturization may require the use of a process compatible with high voltages (for example thick-oxide devices in CMOS, or GaN or SiC processes) for voltage blocking capabilities. Alternatively, it may be possible to integrate the relay bare die into a system-in-package, or employ the use of MEMS-based relays instead.

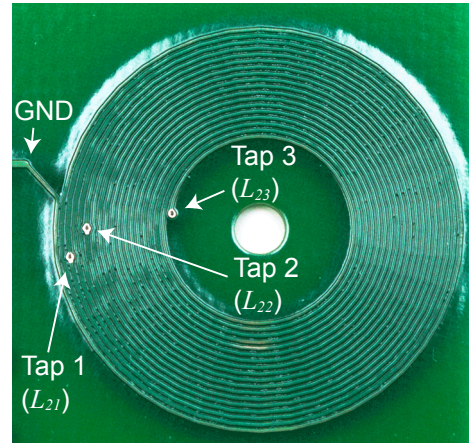


Fig. 7. Photograph of the three-tap secondary coil.

varying k and R_C conditions can present wildly varying impedances as seen by the primary, making the design of uncompensated class-E amplifiers impractical for these cases. To combat this issue, others have described interesting control loops to provide robustness against load variations that offer promising potential [15]. On the other hand, class-D amplifiers can operate reasonably efficiently without significant regard for load impedances. Consequently, such an amplifier was chosen for this initial prototype. Specifically, the amplifier is implemented as an inverter structure with NDS351AN and FDN360P NMOS and PMOS transistors, respectively.

The rectifier is composed of four Panasonic DB2S205 Schottky diodes in a bridge configuration.

2) *Coil Design:* The primary and secondary coils in the discrete prototype are both designed as printed inductors on an FR-4 substrate circuit board. The primary coil is an $N = 8$ turn design, while the secondary coil is an $N = 18$ turn design. In this particular implementation, it was found that two additional taps (at turns 2 and 5) offered sufficient power transfer across the range of expected k (0.05-0.3) and R_L (10-1000 Ω). A photograph of the implemented secondary coil is shown in Fig. 7. Both the primary and secondary coils are printed using 2-oz copper with a trace width/spacing of 0.2 mm. The primary coil is designed with a diameter of 30 mm, while the secondary coil is designed to be slightly smaller at 25 mm for robustness to mis-alignment.

Electromagnetic simulations were performed using Mentor Graphics IE3D to extract inductance and mutual coupling information. A summary of the simulated coil parameters are shown in Table I.

TABLE I
SIMULATED COIL PARAMETERS.

	L_1	L_{21}	L_{22}	L_{23}
N	8	2	5	18
L [μH]	3.31	0.28	1.25	6.73
R_{series} [Ω]	2.02	0.47	1.10	3.07
Q	70	26	48	93
C_{tune} [pF]	167	1954	443	82

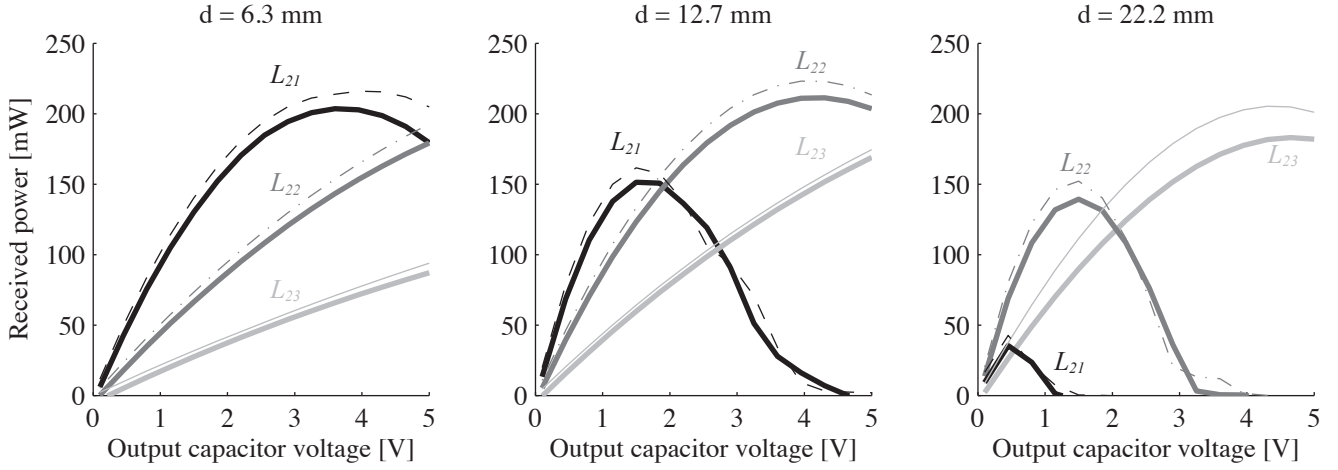


Fig. 8. Power delivered to a Keithley 2400 sourcemeter set at fixed voltage values for a few select distances. The thin curves correspond to a fixed secondary tap configuration (i.e., without any series switches). Here, $V_s = 3.3 V_{p-p}$ and $f = 6.78$ MHz.

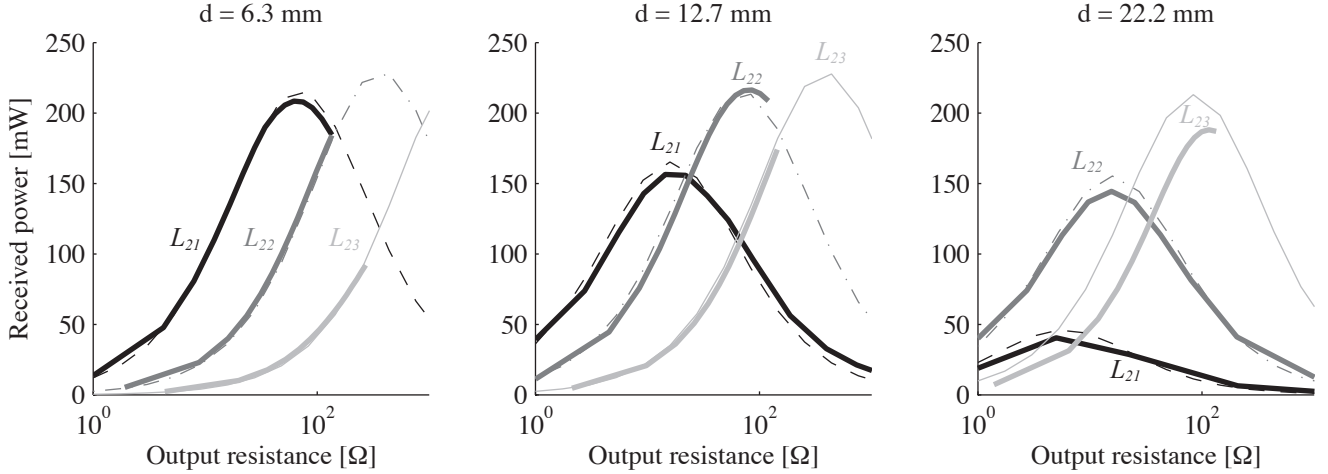


Fig. 9. Measured power delivery compared to analytically predicted power delivery in thick and thin curves, respectively. The abrupt ending of measured curves occur when the capacitor reaches an output voltage of 5 V. Here, $V_s = 3.3 V_{p-p}$ and $f = 6.78$ MHz under measurement conditions, and $L_1 = 3.3 \mu\text{H}$, $L_{21} = 0.28 \mu\text{H}$, $L_{22} = 1.25 \mu\text{H}$, $L_{23} = 6.73 \mu\text{H}$, $Q_{1,eff} = 48$, $Q_{21,eff} = 2.5$, $Q_{22,eff} = 10$, and $Q_{23,eff} = 40$ for analytical calculations (effective Q s lump in R_1 , series switch resistance, and rectifier losses).

IV. MEASUREMENT RESULTS

The inductive coupling system was tested in a typical electronics lab environment using nylon board-spacers of various lengths to separate the primary and secondary coils. Voltage and power monitoring were simultaneously performed using a Keithley 2400 sourcemeter at the output of the rectifier.

Figure 8 demonstrates the benefits of using a multi-tapped secondary coil by measuring received output power: not a single tap configuration offers the best performance across various coil separation distances and output capacitor voltages. At close coil separation distances (i.e., high- k), inductor L_{21} delivers the most power to the load, while inductor L_{23} delivers the most power to the load at long distances (low- k). At intermediate distances, dynamically switching between secondary coil configurations as the output capacitor voltage increases can achieve superior power delivery results. The thin lines in Fig. 8 are measurement results without using the series switches (i.e., a direct connection is instead used). At worse,

the series switches add a 9.7% power loss at maximum power transfer (this includes the 5 mW switch operation power).

The x -axis shown in Fig. 8 is converted to resistance values by dividing the output capacitor voltage by its incoming current; these results are then compared in Fig. 9 to analytical predictions. Measured results match the theoretically predicted behavior very closely for all tap configurations, with the exception of the third tap at long coupling distances, likely due to a coupling coefficient estimation mismatch. Note that the measured output resistance is limited under certain tap and distance configurations due to output capacitor voltage limits.

The implemented inductive coupling circuit was used to demonstrate improved capacitor charging time and range. Figure 10 shows measured transient results of charging a 2.5 F ultra-capacitor to 5 V for coil separation distances of 9.5 mm and 19.2mm. The thin lines correspond to static individual tap configurations, while the thick lines correspond to dynamic switching between taps. Measurements of static individual tap

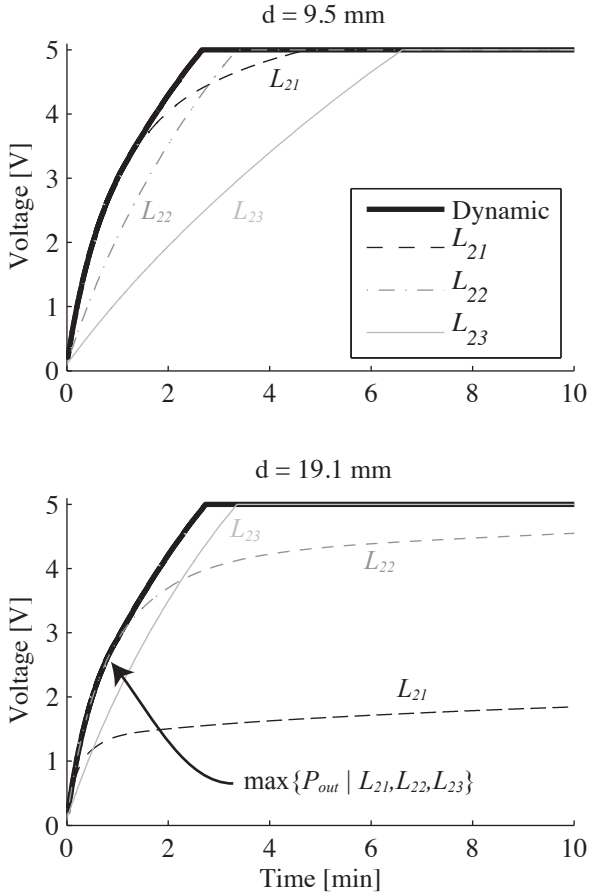


Fig. 10. Transient measurement of charging a 2.5 F ultra-capacitor to 5 V. The thin lines corresponds to exclusive use of inductors L_{21} , L_{22} , and L_{23} , while the thick black line corresponds to dynamic switching between them.

configurations were obtained by removing the series switches (i.e., shorting out a direct connection) to better compare the proposed architecture to conventional approaches.³

In these experiments, a Keithley 2400 sourcemeter was employed as a periodic power meter to determine the optimal inductor tap selection, as shown in Fig. 6b. Specifically, the sourcemeter was connected directly across the ultra-capacitor, while most often operating in a high-impedance voltage-monitoring mode. Periodically, when the output voltage crossed 0.5 V charging thresholds, the sourcemeter would temporarily enter a low-impedance voltage-sourcing, current-sensing mode, while the tap configurations were iterated through (the voltage was set to exactly the current ultra-capacitor state). The tap corresponding to the highest level of received power was selected for operation until the next 0.5 V threshold was reached. In this manner, the circuit was always configured to receive maximum power, so as to charge the load capacitor as rapidly as possible, regardless of any losses in up-stream components. Alternatively, it is instead possible to directly measure the instantaneous load impedance

³Due to a measurement setup limitation, the 5 mW quiescent switch power was not taken into account for charging-time measurements; the lost power consumption was indeed included for power transfer measurements, however.

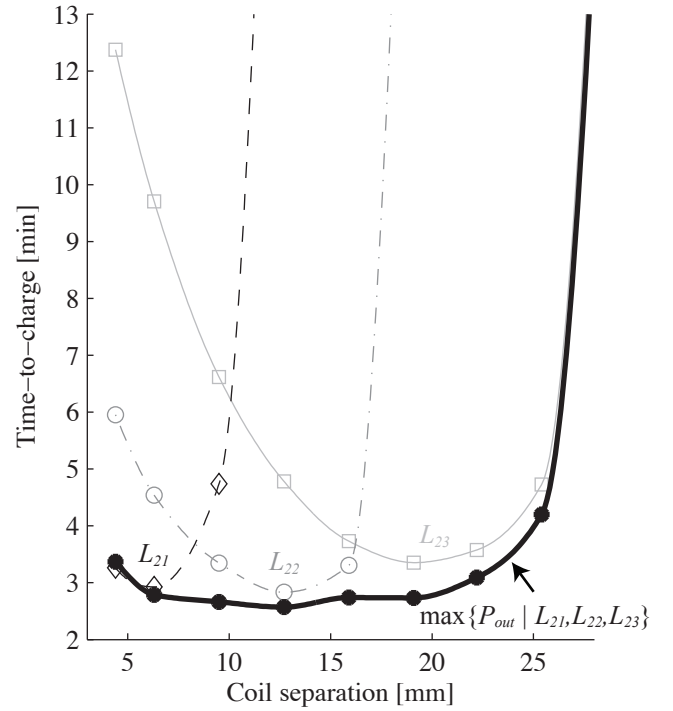


Fig. 11. Charging time for a 2.5 F, 5 V ultra-capacitor. The thin lines corresponds to exclusive use of inductors L_{21} , L_{22} , and L_{23} , while the thick black line corresponds to dynamic switching between them.

in order to match it to the theoretical optimum. However, such an approach would likely require a series sensor, which would not take into account the impedance of up-stream components (the rectifier, for example), while also introducing additional losses. Although the proposed mode of control employing an external sourcemeter is feasible for discrete prototyping, it is not suitable for an IC implementation. Rather than implementing a full power meter, future work on an IC design could instead monitor how rapidly the ultra-capacitor (or a smaller test capacitor) voltage rises for the various tap configurations, thereby directly indicating which tap is optimal for rapid charging.

The charging time and power transfer results for various coil separation distances are summarized in Figure 11 and Table II. In general, inductor L_{21} provides the best performance amongst static configurations at small coil separations distances, inductor L_{22} at medium distances, and inductor L_{23} at long distances. Meanwhile, dynamically switching between all three taps provides superior charging times at nearly all coil separation distances. For example, at a distance of 4.4 mm, dynamic switching achieves a charging time that is 3.7X faster than using inductor L_{23} alone.⁴ At a distance of 12.7 mm, however, inductor L_{21} requires 26 minutes to reach 5V, which is 10.2X slower than the dynamic configuration. Similarly, at a distance of 19.1 mm, inductor L_{21} can no longer charge the load to 5 V, while the dynamic system requires

⁴Interestingly, operating inductor L_{21} alone at 4.4 mm offers fractionally faster charging time than the dynamic configuration, due to reduced resistive losses (owing to the removed series switch for static tap testing).

TABLE II
SUMMARY OF CHARGING TIME AND RESISTIVE SWITCH LOSSES FOR THE DISCRETE PROTOTYPE SYSTEM.

Coil separation distance [mm]	Charging time [minutes]				Maximum charging time improvement [†]	Peak power delivery [‡] [mW]	Maximum series switch resistive loss + quiescent loss at peak power delivery
	L_{21}	L_{22}	L_{23}	Dynamic [†]			
4.4	3.3	6.0	12.4	3.4	3.7X	198 (tap 1)	14.3 + 5.0 = 19.3 mW (9.7%)
6.3	2.9	4.5	9.7	2.8	3.5X	203 (tap 1)	5.3 + 5.0 = 10.3 mW (5.1%)
9.5	4.7	3.3	6.6	2.7	2.4X	216 (tap 2)	6.4 + 5.0 = 11.4 mW (5.3%)
12.7	26.6	2.8	4.8	2.6	10.2X	211 (tap 2)	6.7 + 5.0 = 11.7 mW (5.5%)
19.1	∞^*	22.6	3.3	2.7	∞^* / 8.3X	212 (tap 3)	4.1 + 5.0 = 9.1 mW (4.3%)
22.2	∞^*	∞^*	3.6	3.1	∞^* / 1.2X	183 (tap 3)	16.6 + 5.0 = 21.6 mW (9.1%)

[†] Includes resistive switch losses, but not quiescent switch power consumption losses.

[‡] Includes all switch losses.

* At such coil separations, it is, for all practical purposes, not possible to charge to 5 V. Charging time-improvements in these cases are for the next-best tap configuration.

2.7 minutes – which is 8.3X faster than using inductor L_{22} in a static configuration. As a result of the dynamic inductor reconfigurability, the operational range of the system whereby the ultra-capacitor is charged to 5 V in a reasonable amount of time is expanded by upwards of 2.5X.

V. CONCLUSIONS

The goal of this work was to provide, through an inductively coupled link, maximum power to a load capacitor in order to charge it as rapidly as possible. Although analysis of inductive coupling theory is conventionally performed to optimize efficiency or link gain, this paper instead presented analysis used to maximize power transfer to the load. It was found that given coil geometries and separation distances, there exists a load resistance that maximizes power transfer. Since a charging capacitor can be modeled as an instantaneously increasing impedance, there exists at most one point in time during the capacitor charging interval where maximum power is being delivered. However, it was also found that the optimal load impedance can be modified by adjusting the ratio of secondary reactances. As a result, this paper presented a multi-tapped secondary coil whose inductance and resonant tuning capacitance could be dynamically adjusted in order to deliver maximum power to the load over a wider range of output impedances and coil separation distances. Measurement results verified the feasibility of this concept, demonstrating an inductive link that operated over a 2.5X longer range while charging an ultra-capacitor up to several times faster than conventional approaches.

Although the analysis and experimental results were optimized for maximizing power transfer, the efficiency of an inductive link also has a maximum at a single optimal load impedance that depends on the ratio of secondary reactances (as shown in the Appendix). It could thus be possible for future work to extend the multi-tapped architecture to systems that require high efficiency over variable load or coil separation conditions.

ACKNOWLEDGMENTS

The authors acknowledge the support of the C2S2 Focus Center, one of six research centers funded under the Focus Center Research Program (FCRP), a Semiconductor Research Corporation entity. The authors thank Benjamin Tay, Sushmit

Goswami, and Phillip Nadeau for preliminary testing and support.

VI. APPENDIX - EFFICIENCY ANALYSIS

The maximum power transfer analysis developed in Section II-B can be leveraged to also derive optimal efficiency criteria. Total link efficiency can be broken out into two separate components: primary and secondary efficiencies. Specifically, the circuits in Figures 4(d) and 4(a) can be used to calculate the primary and secondary efficiencies at resonance, respectively.

$$\begin{aligned}
 \eta_{tot} &= (\eta_1) \times (\eta_2) \\
 &= \left(\frac{R_{eq}}{R_{eq} + R_s + R_1} \right) \times \left(\frac{R_L}{R_L + R_2} \right) \\
 &= \dots (\text{lumping } R_s \text{ together with } Q_1, \rightarrow Q_1 = \frac{\omega L_1}{R_1 + R_s}) \\
 &= \frac{k^2 Q_1 \omega C_2 R_L}{\left(\omega C_2 R_L + k^2 Q_1 + \frac{1}{Q_2} \right) \left(\omega C_2 R_L + \frac{1}{Q_2} \right)} \quad (11)
 \end{aligned}$$

Taking the derivative of efficiency with respect to R_L and equating to zero will yield the load impedance that maximizes power transfer efficiency:

$$R_{L, \eta_{opt}} = \sqrt{\frac{L_2}{C_2}} \left(\frac{\sqrt{1 + k^2 Q_1 Q_2}}{Q_2} \right). \quad (12)$$

Similar results were also derived in [15], [17]. For completeness, the optimal efficiency given this result is shown here:

$$\eta_{opt} = \frac{k^2 Q_1 Q_2}{(1 + \sqrt{1 + k^2 Q_1 Q_2})^2}. \quad (13)$$

What is very interesting to note here is that the $R_{L, \eta_{opt}}$ expression is identical to the $R_{L, opt}$ expression for maximum power transfer, with the only difference being the square root of $(1 + k^2 Q_1 Q_2)$ in the numerator.

Since the optimal load impedance for efficiency is also dependent on the ratio of secondary reactances, the multi-tap architecture presented in this paper could also be used to improve efficiency over a wider range of output impedances or coupling coefficients. For example, Fig. 12 shows the efficiency of wireless power transfer for various k and L_2 , given a fixed load impedance. It can be seen that at a given coupling coefficient, one of the three taps will offer superior power transfer efficiency. Naturally, such a technique could be

combined with a primary-side supply modulation technique to deliver the appropriate amount of power at the highest possible efficiency [29].

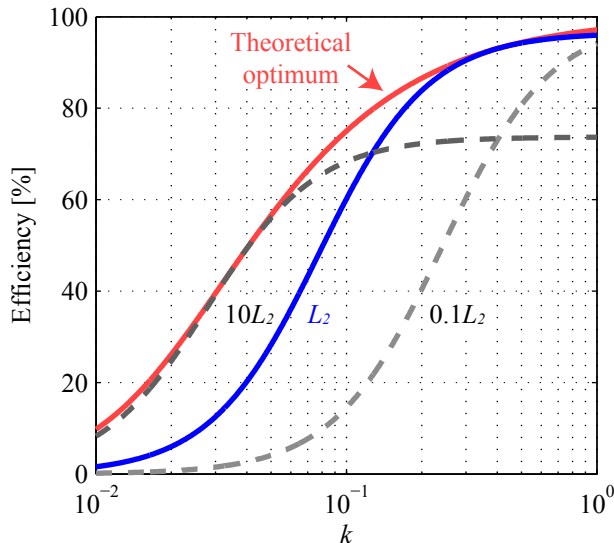


Fig. 12. Wireless power transfer efficiency under the same conditions as shown in Fig. 5, for a load impedance $R_L = 100 \Omega$ and various values of L_2 . The solid red curve is the theoretically maximal efficiency under optimal conditions for each value of k .

REFERENCES

- [1] H. McDermott, "An advanced multiple channel cochlear implant," *IEEE Trans. Bio-Med. Eng.*, vol. 36, no. 7, pp. 789–797, 1989.
- [2] R. Harrison, P. Watkins, R. Kier, R. Lovejoy, D. Black, B. Greger, and F. Solzbacher, "A low-power integrated circuit for a wireless 100-electrode neural recording system," *IEEE J. Solid-State Circuits*, vol. 42, no. 1, pp. 123–133, 2007.
- [3] K. Finkenzeller, *RFID handbook: Fundamentals and applications in contactless smart cards, radio frequency identification and near-field communication*. Wiley, 2010.
- [4] C. Sellathamby, M. Reja, L. Fu, B. Bai, E. Reid, S. Slupsky, I. Filanovsky, and K. Iniewski, "Noncontact wafer probe using wireless probe cards," in *Proc. IEEE Int. Test Conf.* IEEE, Nov. 2005.
- [5] C. Kim, D. Seo, J. You, J. Park, and B. Cho, "Design of a contactless battery charger for cellular phone," *IEEE Trans. Ind. Electron.*, vol. 48, no. 6, pp. 1238–1247, 2001.
- [6] X. Jian and H. Yu, "A novel wireless charging system for movable telephone with printed-circuit-board windings of different structure and shape respectively," in *Proc. IEEE Int. Conf. Elec. Machines Systems*, 2007, pp. 1283–1285.
- [7] D. Yeager, P. Powlledge, R. Prasad, D. Wetherall, and J. Smith, "Wirelessly-charged uhf tags for sensor data collection," in *Proc. IEEE Int. Conf. RFID*, 2008, pp. 320–327.
- [8] N. Shinohara and H. Matsumoto, "Wireless charging system by microwave power transmission for electric motor vehicles," *IEICE Trans. Electronics*, vol. 87, pp. 433–443, 2004.
- [9] A. Burke, "Ultracapacitors: why, how, and where is the technology," *Journal of Power Sources*, vol. 91, no. 1, pp. 37–50, 2000.
- [10] "ML2020 Data Sheet," Panasonic, 2005.
- [11] "UltraCap8 Series ESHSR-0003C0-002R7 Data Sheet," NessCap Ultracapacitors, 2008.
- [12] C. Liu, Z. Yu, D. Neff, A. Zhamu, and B. Jang, "Graphene-based supercapacitor with an ultrahigh energy density," *Nano Letters*, vol. 10, pp. 4863–4868, 2010.
- [13] A. Pandey, F. Allos, A. Hu, and D. Budgett, "Integration of supercapacitors into wirelessly charged biomedical sensors," in *Proc. IEEE Conf. on Indust. Elec. Applications*, 2011, pp. 56–61.
- [14] W. Sanchez, C. Sodini, and J. Dawson, "An energy management IC for bio-implants using ultracapacitors for energy storage," in *Proc. IEEE Symp. VLSI Circuits*, 2010, pp. 63–64.
- [15] R. Sarpeshkar, *Ultra Low Power Bioelectronics: Fundamental, Biomedical Applications, and Bio-Inspired Systems*. Cambridge, UK: Cambridge University Press, 2010.
- [16] R. Harrison, "Designing efficient inductive power links for implantable devices," in *Proc. IEEE ISCAS*, May 2007, pp. 2080–2083.
- [17] K. Van Schuylenbergh and R. Puers, *Inductive Powering: Basic Theory and Application to Biomedical Systems*. Springer, 2009.
- [18] E. Sakai and H. Sakamoto, "Wireless Rapid Charger of Super Capacitor," *PRZEGLD ELEKTROTECHNICZNY (Electrical Review)*, no. 6, pp. 114–117, 2012.
- [19] S. Kim, K.-S. No, and P. H. Chou, "Design and Performance Analysis of Supercapacitor Charging Circuits for Wireless Sensor Nodes," *IEEE J. Emerging and Selected Topics in Circuits and Systems*, vol. 1, no. 3, pp. 391–402, Sep. 2011.
- [20] T. H. Lee, *The Design of CMOS Radio-Frequency Integrated Circuits, 2nd ed.* Cambridge, UK: Cambridge University Press, 2004.
- [21] K. Van Schuylenbergh and R. Puers, "Self-tuning inductive powering for implantable telemetric monitoring systems," *Sensors and Actuators A: Physical*, vol. 52, no. 1, pp. 1–7, 1996.
- [22] A. Kurs, A. Karalis, R. Moffatt, J. Joannopoulos, P. Fisher, and M. Soljačić, "Wireless power transfer via strongly coupled magnetic resonances," *Science*, vol. 317, no. 5834, pp. 83–86, 2007.
- [23] M. Kiani and M. Ghovanloo, "The Circuit Theory Behind Coupled-Mode Magnetic Resonance-Based Wireless Power Transmission," *IEEE Trans. Circuits Syst. I*, no. 99, pp. 1–1, 2012.
- [24] R. Shaffer, *Fundamentals of power electronics with MATLAB*. Boston, MA: Charles River Media, 2007.
- [25] T. Beh, T. Imura, M. Kato, and Y. Hori, "Basic study of improving efficiency of wireless power transfer via magnetic resonance coupling based on impedance matching," in *Proc. Int. Symp. Industrial Electronics*, 2010, pp. 2011–2016.
- [26] A. Tanabe, K. Hijioka, H. Nagase, and Y. Hayashi, "A Novel Variable Inductor Using a Bridge Circuit and Its Application to a 5–20 GHz Tunable LC-VCO," *IEEE J. Solid-State Circuits*, vol. 46, no. 4, pp. 883–893, 2011.
- [27] C. Fu, C. Ko, C. Kuo, and Y. Juang, "A 2.4–5.4-GHz wide tuning-range CMOS reconfigurable low-noise amplifier," *IEEE Trans. Microw. Theory Tech.*, vol. 56, no. 12, pp. 2754–2763, 2008.
- [28] M. Paernel, "High-efficiency transmission for medical implants," *IEEE Solid-State Circuits Magazine*, vol. 3, no. 1, pp. 47–59, 2011.
- [29] G. Wang, W. Liu, M. Sivaprakasam, and G. Kendir, "Design and analysis of an adaptive transcutaneous power telemetry for biomedical implants," *IEEE Trans. Circuits Syst. I*, vol. 52, no. 10, pp. 2109–2117, Oct. 2005.

PLACE
PHOTO
HERE

Patrick P. Mercier (S'04-M'12) received the B.Sc. degree in electrical and computer engineering from the University of Alberta, Edmonton, AB, Canada, in 2006, and the S.M. and Ph.D. degrees in electrical engineering and computer science from the Massachusetts Institute of Technology (MIT), Cambridge, MA, in 2008 and 2012, respectively.

He is currently an Assistant Professor at the University of California, San Diego, in the department of Electrical and Computer Engineering. His research interests include the design of energy-efficient digital systems, RF circuits, power converters, and sensor interfaces for biomedical and implantable applications.

Prof. Mercier was a co-recipient of the 2009 ISSCC Jack Kilby Award for Outstanding Student Paper at ISSCC 2010. He also received a Natural Sciences and Engineering Council of Canada (NSERC) Julie Payette fellowship in 2006, NSERC Postgraduate Scholarships in 2007 and 2009, and an Intel Ph.D. Fellowship in 2009.

PLACE
PHOTO
HERE

Anantha P. Chandrakasan (F'04) received the B.S., M.S. and Ph.D. degrees in Electrical Engineering and Computer Sciences from the University of California, Berkeley, in 1989, 1990, and 1994 respectively. Since September 1994, he has been with the Massachusetts Institute of Technology, Cambridge, where he is currently the Joseph F. and Nancy P. Keithley Professor of Electrical Engineering.

He was a co-recipient of several awards including the 1993 IEEE Communications Society's Best Tutorial Paper Award, the IEEE Electron Devices Society's 1997 Paul Rappaport Award for the Best Paper in an EDS publication during 1997, the 1999 DAC Design Contest Award, the 2004 DAC/ISSCC Student Design Contest Award, the 2007 ISSCC Beatrice Winner Award for Editorial Excellence and the ISSCC Jack Kilby Award for Outstanding Student Paper (2007, 2008, 2009). He received the 2009 Semiconductor Industry Association (SIA) University Researcher Award. He is the recipient of the 2013 IEEE Donald O. Pederson Award in Solid-State Circuits.

His research interests include micro-power digital and mixed-signal integrated circuit design, wireless microsensor system design, portable multimedia devices, energy efficient radios and emerging technologies. He is a co-author of *Low Power Digital CMOS Design* (Kluwer Academic Publishers, 1995), *Digital Integrated Circuits* (Pearson Prentice-Hall, 2003, 2nd edition), and *Sub-threshold Design for Ultra-Low Power Systems* (Springer 2006). He is also a co-editor of *Low Power CMOS Design* (IEEE Press, 1998), *Design of High-Performance Microprocessor Circuits* (IEEE Press, 2000), and *Leakage in Nanometer CMOS Technologies* (Springer, 2005).

He has served as a technical program co-chair for the 1997 International Symposium on Low Power Electronics and Design (ISLPED), VLSI Design '98, and the 1998 IEEE Workshop on Signal Processing Systems. He was the Signal Processing Sub-committee Chair for ISSCC 1999-2001, the Program Vice-Chair for ISSCC 2002, the Program Chair for ISSCC 2003, the Technology Directions Sub-committee Chair for ISSCC 2004-2009, and the Conference Chair for ISSCC 2010-2012. He is the Conference Chair for ISSCC 2013. He was an Associate Editor for the IEEE Journal of Solid-State Circuits from 1998 to 2001. He served on SSCS AdCom from 2000 to 2007 and he was the meetings committee chair from 2004 to 2007. He was the Director of the MIT Microsystems Technology Laboratories from 2006 to 2011. Since July 2011, he is the Head of the MIT EECS Department.